Journal of Applied Physics

Phonon variations in nano-crystalline lutetium sesquioxide under the influence of varying temperature and pressure

Cite as: J. Appl. Phys. **126**, 245901 (2019); https://doi.org/10.1063/1.5125702
Submitted: 25 August 2019 . Accepted: 07 December 2019 . Published Online: 27 December 2019

Neha Bura, Deepa Yadav, Jasveer Singh, and Nita Dilawar Sharma

Journal of Applied Physics ARTICLE scitation.org/journal/jap

Phonon variations in nano-crystalline lutetium sesquioxide under the influence of varying temperature and pressure

Cite as: J. Appl. Phys. **126**, 245901 (2019); doi: 10.1063/1.5125702
Submitted: 25 August 2019 · Accepted: 7 December 2019 ·
Published Online: 27 December 2019

Neha Bura,[1,2] Deepa Yadav,[1,2] Jasveer Singh,[1] and Nita Dilawar Sharma[1,2,a)]

AFFILIATIONS

[1]Pressure, Vacuum & Ultrasonic Metrology Section, Physico-Mechanical Metrology Division, CSIR-National Physical Laboratory, New Delhi 110012, India
[2]Academy of Scientific and Innovative Research (AcSIR), Ghaziabad 201002, India

[a)]ndilawar@nplindia.org

ABSTRACT

This manuscript reports temperature-dependent Raman studies on nanocrystalline lutetium sesquioxide for a temperature range of 80–420 K. Phase stability under pressure was also investigated up to a pressure of about 15.6 GPa, primarily to deduce the mode Grüneisen parameters, which were further used to estimate the anharmonic parameters under the influence of varying sample temperature. The characterization at ambient revealed the cubic phase and nanocrystalline nature of the sample. The variation in the Raman shift and FWHM studied with an increase in temperature revealed that a few new peaks started developing above about 220 K, which were, unexpectedly, found to be due to the cubic phase of the material. On the other hand, it was observed that with an increase in pressure, the cubic phase peaks appear to be destabilized and new broad bands started to develop. However, until the highest studied pressure of 15.6 GPa, a defined structural phase transition was not observed. The estimated anharmonic constants demonstrated the predominance of the three phonon process in phonon decay as a function of temperature.

INTRODUCTION

Rare earth sesquioxides have gained much importance due to their various applications in corrosion-resistant electrical insulation layers,[1] grain growth inhibitors,[2] light-emitting diodes,[3] solid-state laser rods,[4] solid oxide fuel cells,[5] optical materials,[6] and many more. These rare earth oxides exist in three structural phase modifications—cubic with the space group *Ia-3* (206) and denoted by C, monoclinic with the space group *C2/m* (12) and denoted by B, hexagonal with the space group *P-3m1* (164) and denoted by A. At elevated temperatures, two additional phases, i.e., cubic with the space group *Im-3m* (229) and denoted by X and hexagonal with the space group $P6_3/mmc$ (194) and denoted by H, are also exhibited by rare earth sesquioxides. At ambient, most rare earth oxides exhibit a cubic crystal structure with the space group *Ia-3* having two local symmetries, i.e., C_2 and C_{3i}, and having 16 molecules per unit cell.[7] The structure has 24 Lu^{3+} ions on-site with the C_2 symmetry and eight on-site with the C_{3i} symmetry.[8]

Among these rare earth oxides, lutetium oxide (Lu_2O_3) has recently been shown to have many strategic and prospective applications owing to its potentially excellent thermal stability, insulating property due to a large bandgap of 5.5 eV, hygroscopic immunity, high lattice energy, etc. Lu_2O_3 has recently gained importance as it can be used as a catalyst in many alkylation,[9] hydrogenation, cracking, and polymerization processes and as a scintillator due to its transparency,[10] to produce white light using frequency up-conversion,[11] to make ultrafast laser materials,[12] and various other applications. It is also an essential raw material for laser crystals.[4] It also has specialized uses in vacuum deposition, ceramics, glass, and phosphors. Tm:Lu_2O_3 nanocrystals have shown potential for phosphor blue applications.[13] In recent years, Dy:Lu_2O_3 has also been shown to be a suitable material for midinfrared lasers.[14] Lu_2O_3:Eu^{3+} has the potential for use as a scintillator for x-ray imaging applications.[15] Hence, due to such technological and fundamental importance of Lu_2O_3, it is essential to study the phase stability of these materials with pressure and temperature, especially

nanosized Lu_2O_3, since under extreme conditions, a number of phenomena such as a change in the crystal structure as well as electronic and thermodynamic properties can impact the performance of the devices made out of this promising material.[16,17]

In the past few years, structural investigations have been done on Lu_2O_3 by several researchers to unmask the crystal structure and stability of the material[18–20] and its dielectric properties.[21] However, there are very few investigations under the application of extreme conditions. Hoekstra reported a cubic to monoclinic transformation in Lu_2O_3 at 3.6 GPa and 1000 °C.[7] Recently, the stability of the cubic phase was estimated to be above 3000 °C.[22] Jiang *et al.*[23] investigated the pressure-induced phase transitions using the x-ray and Raman spectroscopy and demonstrated a cubic to monoclinic transition above a pressure of about 12.7 GPa. However, Lin *et al.* observed the commencement of cubic to monoclinic transition at about 17 GPa.[24] To the best of our knowledge, no other reports on the effect of temperature and pressure are available, more so, for the nanocrystalline sample and anharmonic parameters. Hence, in this report, we investigate the temperature-dependent change shown by nanocrystalline Lu_2O_3 in terms of the shift in the phonon modes and change in their widths at half maxima. The mode Grüneisen parameter estimated from the pressure behavior of the sample was used to determine the anharmonic constants and the anharmonicity contributions.

MATERIALS AND METHODS

The nanocrystalline powder sample of Lu_2O_3, procured from Johnson Matthey, UK, was used as the starting material. The sample was used in as-received state and not subjected to any pretreatments. Characterization at ambient was carried out using x-ray diffraction, scanning electron microscopy, energy dispersive x-ray analysis, and Raman spectroscopy. X-ray diffraction was carried out using the Rigaku Ultima-IV X-Ray Diffractometer with Cu kα ($\lambda = 1.5404$ Å) radiation. A scan of 0.067°/s was performed for recording the diffractograms with a step size of 0.02°.

For the micro-Raman measurements, a Jobin Yvon made T64000 Triple Raman spectrometer was used. An argon-ion laser with a wavelength of 514.5 nm was used as the excitation source with a power of 100 mW at the source. The laser was focused on the sample using the microscope with a 20× objective. The back-scattered beam from the sample was collected by a charge coupled device (CCD), and the collected scattering pattern was integrated into Intensity count vs Raman shift using LabSpec Software.

The Raman spectra were collected for a temperature range of 80 K–420 K. A pellet of 3 mm diameter of Lu_2O_3 was made using an indigenously constructed die. For the temperature measurements, a Janis made, continuous flow liquid nitrogen cryostat ST-500 was used with a temperature controller working in the temperature range mentioned above. The sample was loaded in the sample chamber of the cryostat, and a vacuum on the order of 10^{-6} was maintained in the sample chamber using a turbomolecular pump.

For high-pressure measurements, the pressure on the sample was applied using the Almax Laboratories made Diacell Maxi, a Mao-Bell type diamond anvil cell (DAC) with 400 μm culets. The sample was loaded in a stainless steel gasket with 100 μm hole along with a few ruby chips, which was used as the pressure monitor, and a mixture of methanol and ethanol in a 4:1 ratio as the pressure transmitting medium.

RESULTS AND DISCUSSION

Characterization at ambient

The XRD result was used for the qualitative analysis. The experimentally obtained data, as shown in Fig. 1, is compared with the reference data and agrees well with the JCPDS Card No. 430121, which corresponds to the cubic phase of the material with the space group *Ia-3(206)*. Miller indices of the peaks are also specified in the figure. No other peaks in the diffraction pattern other than the peaks of the cubic Lu_2O_3 were observed. The crystallite size of the material was also calculated using the Debye–Scherrer formula using the predominating peak at $2\theta = 29.75°$ (±0.5°), which comes out to be 34.88 nm, showing that the material is nanocrystalline.

The Rietveld analysis of the obtained data was done to confirm the phase of the sample. The result obtained is shown in Fig. 2. The circles represent the experimental data, the red line represents the calculated data, the blue line represents the agreement between the experimental and observed data, and the pink lines represent the angles at which Bragg's law is satisfied. The Rietveld analysis was done using the FullProf software.

Scanning electron microscopy (SEM) was done for the surface morphology of the sample, and the obtained micrographs are shown in Fig. 3 displaying faceted crystalline particles with predominant particle sizes in the nanometer range.

Furthermore, the compositional analysis of the material is carried out using energy dispersive x-ray spectroscopy (EDS). The EDS results give the atomic and weight percentage of the elements present in the sample. According to the stoichiometric weight percentage of Lu_2O_3, 12.06% of oxygen and 87.9% of lutetium must be present, while according to the atomic percentage, 60% of oxygen and 40% of lutetium is expected. In our case, as shown in Fig. 4, the obtained results agree well with the theoretical results, albeit

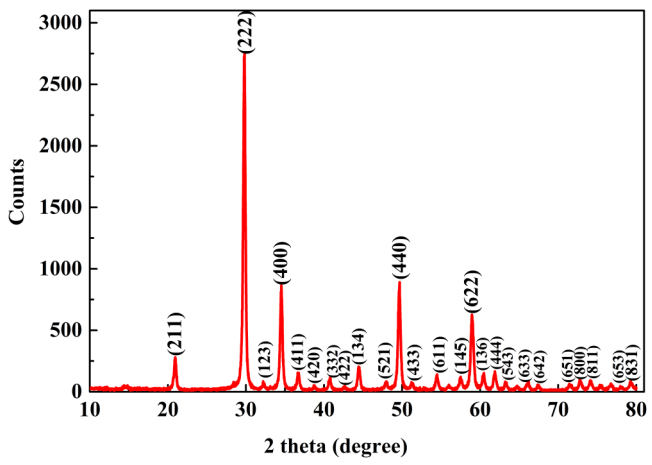

FIG. 1. XRD results of Lu_2O_3.

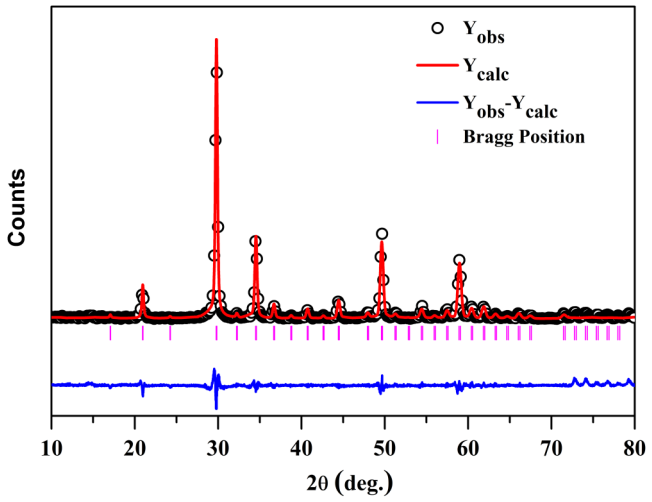

FIG. 2. Rietveld analysis of the XRD results. rp, rwp, re, and chi-square are 22.5, 29.9, 16.3, and 3.380, respectively.

with slight deviations. No other contaminations/elements were detected within the sensitivity of the measurement.

From the factor group analysis, there are 22 Raman active modes,[25,] i.e., 4 A_g modes, 4 E_g modes, and 14 F_g modes corresponding to the cubic phase of Lu_2O_3. Under ambient conditions, we observed only 11 modes that are possibly because of the fact that some of the modes are closely placed, and hence they overlap with each other and are not separable. The Raman spectrum taken at ambient conditions is shown in Fig. 5.

The major peak observed, i.e., the peak with the highest intensity centered at 393.1 cm^{-1} is identified as the characteristic peak of the cubic phase and corresponds to the $F_g + A_g$ mode.[26] The other modes observed at 335.1, 348.2, 454.6, 499.1, 603.9, and 613.9 cm^{-1} designated as I_4, I_5, I_8, I_9, I_{10}, and I_{11}, respectively, are also identified as cubic phase peaks.[23,27,28] However, a few additional modes were also observed at 191.2, 229.1, 288.9, and 441.3 cm^{-1}, i.e., I_1, I_2, I_3, and I_7, which have been reported previously only for cubic single crystals by Laversenne *et al.*[29] It is worth mentioning here that the most dominant cubic phase peak, I_6, along with most other modes have been found to be in excellent agreement with the reported positions by Laversenne *et al.*[29] for a single crystal, although our sample is nanocrystalline in nature. The detailed peak identifications, along with their assignments, are given in Table I. The strongest cubic Raman mode identified as I_6, with the largest polarizability change, is expected to be most sensitive to the external influences and is tracked primarily along with other observable modes.

Pressure-dependent phonon variations

Pressure-dependent Raman studies were carried out using DAC up to a pressure of about 15.6 GPa. Figure 6 shows the evolution of various phonon modes in the pressure-dependent Raman spectra. From phonon variations, it is observed that with an

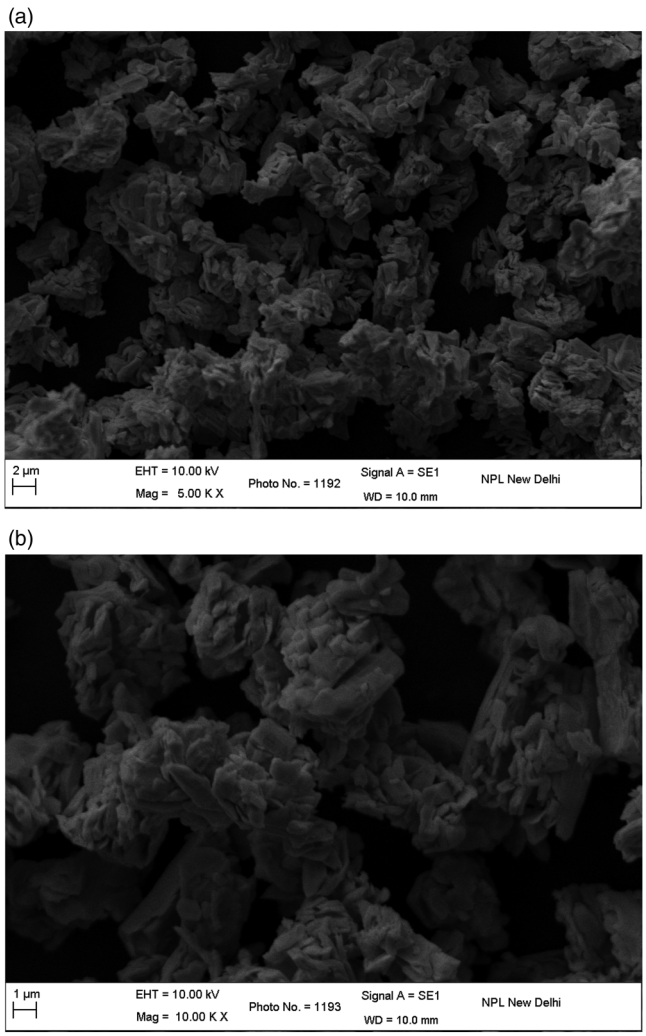

FIG. 3. SEM images of Lu_2O_3.

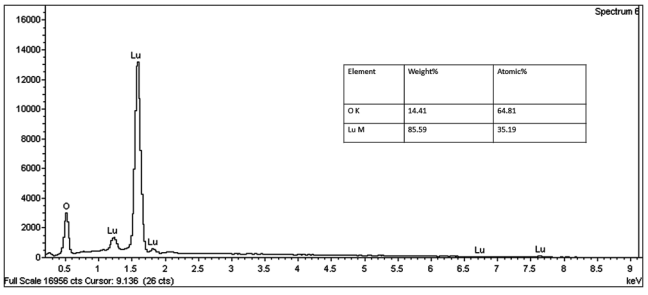

FIG. 4. EDS profile for Lu_2O_3.

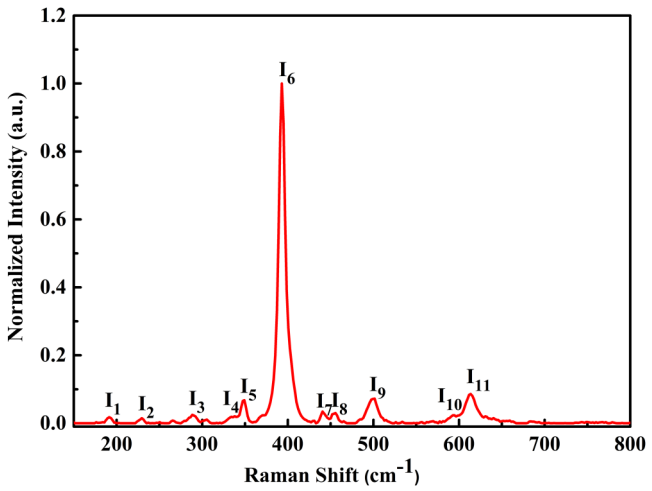

FIG. 5. Raman spectrum of Lu_2O_3 at ambient conditions.

increase in the applied pressure, the cubic phase peaks shift to higher wavenumbers, their width increases, and the peaks lose intensity. However, up to the highest studied pressure, the cubic phase is still existent, albeit new broad bands are seen to be developing between 500 and 700 cm^{-1}, beyond a pressure of about 7 GPa. At the highest pressure of about 15.6 GPa, the most intense $F_g + A_g$ cubic phase mode, I_6, shifts to 423 cm^{-1} from 393.1 cm^{-1} at ambient.

TABLE I. Observed Raman modes at ambient temperature and pressure.

Peak identification	Peak position at 300 K (cm^{-1})	Mode assignment[22]
I_1	191.2	
I_2	229.1	
I_3	288.9	$F_g + E_g$
I_4	335.1	F_g
I_5	348.2	$F_g + E_g$
I_6	393.1	$F_g + A_g$
I_7	441.3	
I_8	454.6	$F_g + E_g$
I_9	499.1	$F_g + A_g$
I_{10}	603.9	$F_g + E_g$
I_{11}	613.9	$F_g + A_g$

Furthermore, the weaker modes of the cubic phase, which were observable at ambient and low pressures, were not found to be clearly observable at higher pressures beyond about 7 GPa, which indicates that the destabilization of the cubic phase started. In addition, the development of the new broad bands around 500–700 cm^{-1} above a pressure of about 7 GPa was not accompanied by the appearance of other well defined peaks. In this context, there is only one report by Jiang *et al.*[23] who reported the initiation of a cubic to monoclinic phase transition at about 12.7 GPa, which completed at 18.2 GPa. Jiang *et al.*[23] also observed the development of broad bands between 500 and 700 cm^{-1} along with new peaks at lower wavenumbers. In our case, the similar commencement of the

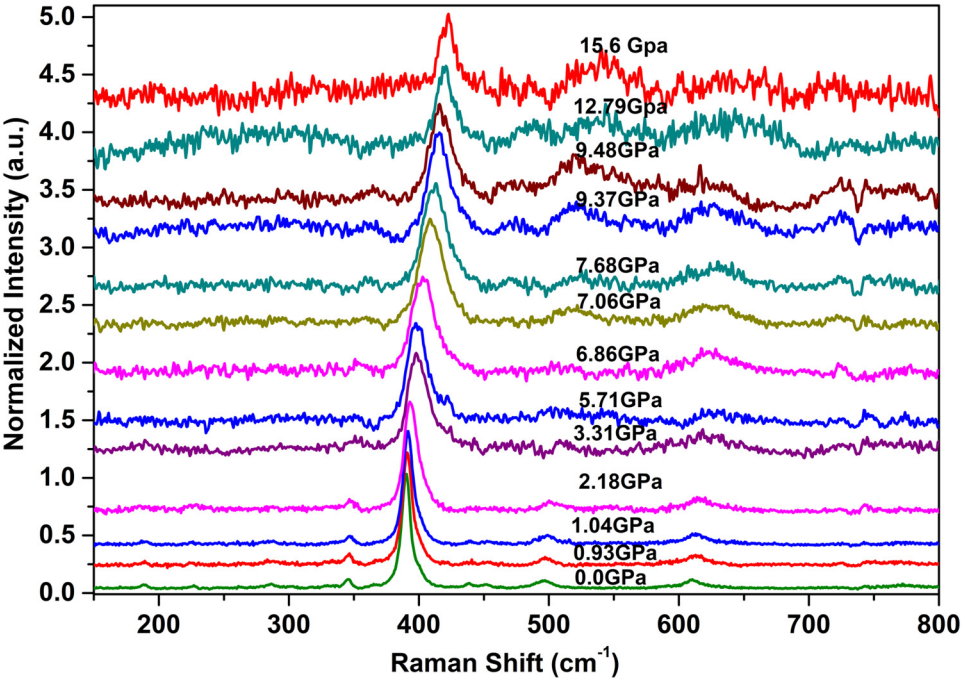

FIG. 6. Raman spectra at various pressure values.

development of broad bands is observed, although up to the highest studied pressure, these newly developed broad bands do not become sharper, and, moreover, no bands were seen to be developing at lower wavenumbers. The signal to noise ratio also reduces, which is expected since with the application of pressure, the sample, which is in micrometer size, disperses. Also, the mixture of methanol and ethanol, which is used as the pressure transmitting medium, is known to remain hydrostatic up to a pressure of about 10.5 GPa only.[30] Beyond this, the pressure is expected to be nonhydrostatic, which may also impact the experimental observations. However, since the broad bands between 500 and 700 cm^{-1} were observed below the hydrostatic limit, they are clearly a consequence of the applied pressure in the present case. Thus, we may surmise that the sample is more or less progressing toward a disordered/amorphous phase notwithstanding the nonhydrostaticity as well as decreased signal to noise ratio with an increase in the applied pressure.

The observance of such a behavior may have a contribution from the fact that the starting sample is nanocrystalline in nature. As reported in our previous work on rare earth sesquioxides,[31] solid-state amorphization is controlled by the relative energies of the defected crystalline phase G_c and the amorphous phase. Although the quantitative estimation of these quantities is not always feasible, however, in case of nanocrystalline materials, the free energy due to defects G_d is known to increase due to the increased volume fraction of grain boundaries and hence the structural transition to disordered or amorphous phase may be preferred owing to the fact that G_a, the free energy of amorphous phase, may become lower than $G_c + G_d$, the free energies of the crystalline phase and defects, respectively. Also, the structural transition from cubic to monoclinic phase involves a large volume change of about 8%–9%, and such transitions have been reported to proceed via the formation of an intermediate phase such as a disordered or amorphous state.[31] Moreover, the cubic phase peaks still exist up to the highest pressure of 15.6 GPa, with no additional well defined peaks due to any other crystalline phase, which shows that the structural evolution, though initiated, is not complete. Hence, we may surmise that beyond a pressure of about 7 GPa, the cubic phase starts destabilizing with weakening of the Raman modes.

In addition, from the variation of the frequency of the phonon modes with respect to the pressure applied, the value of the mode Grüneisen parameter is estimated. The mode Grüneisen parameter is given by

$$\gamma = \frac{d\omega}{dp}\frac{B_0}{\omega_0}. \quad (1)$$

B_0 is the bulk modulus of the elasticity for the cubic phase whose value is taken from the literature,[23] ω_0 is the frequency of the mode at ambient, and $d\omega/dp$ represents the slope of the graph between frequency shift and applied pressure.

Table II shows the calculated values of the mode Grüneisen parameters for the modes that had observable shifts. The $d\omega/dp$ values were calculated up to a pressure range of 15.6 GPa for mode I_6. Since the weaker modes were not clearly distinguishable above a pressure of 7.68 GPa, the slope for these modes was considered up to 7.68 GPa only. As can be seen from the table, as compared to the reported values,[23] the values obtained in the present estimations are consistently lower. These lower values are a direct consequence of the lower values of $d\omega/dp$ for our sample (as shown in Table II) as compared to those reported by Jiang *et al.*[23] Although it appears anomalous, it is not entirely unexpected since it may again be a consequence of the nano nature of the sample, which leads to an increase in surface energy. In this context, Liu *et al.*[32] reported that as a consequence of the reduction in the size of their CeO_2 sample, the sample was more stable as compared to the bulk under the application of external pressure, which was again attributed to the higher surface energy in the nanosized sample.

TABLE II. Calculated mode Grüneisen parameter values for Raman modes of Lu_2O_3.

Peak identification	ω_0 (cm^{-1})	$d\omega/dp$ (cm^{-1}/GPa)	B_0 (GPa)[23]	Calculated γ	Reported γ[23]
I_5	345.1	2.05	214	1.30	1.60
I_6	390.4	2.45		1.35	1.63
I_9	496.1	2.82		1.22	1.90
I_{11}	610.6	2.27		0.81	1.46

Temperature-dependent variations in phonon modes

Figure 7 shows the Raman spectrum of Lu_2O_3 at 80 K, and the inset shows the overlaid spectra at 80 K and 420 K for comparison purposes. It may be observed that at 80 K, only 7 peaks were observed in contrast to 11 modes at ambient and higher temperatures, although the former are sharper with lower FWHM as compared to the peaks at 420 K. However, the observation that lesser number of modes are observed at 80 K is unexpected since the phonon modes at low temperatures are expected to be enhanced and well defined due to lowering of thermal effects.[33,34]

The progression in the cubic phase Raman peaks with an increase in the temperature from 80 K to 420 K is shown in Fig. 8. It may be observed from the figure that although at 80 K only 7 of the 11 Raman modes were observed, as the temperature increased above 220 K, a few other modes designated as I_1, I_2, I_3, and I_7 start appearing in the spectra as already discussed above and are shown in detail in Fig. 9. With the increasing temperature, the phonon modes also show softening to lower wavenumbers, while the intensity of the modes I_1, I_2, I_3, and I_7, at around 180, 227, 290, and 441 cm^{-1}, respectively, increases significantly with increasing temperature. At 340 K and above, the newly developed modes become stronger, while, on the other hand, the relative intensity of the modes I_8 and I_{10} centered at around 455 and 595 cm^{-1}, respectively, decreases. As discussed earlier, the newly emerging peaks were also identified with the cubic phase as reported by Laversenne *et al.*[29] for single crystals. These observations suggest that with an increase in temperature, some kind of reorientation of the cubic structure takes place, which is indicative of either an increased order in the structure or an isostructural transition in the sample. Recently, Jiang *et al.* reported a similar isostructural transition under the application of pressure in

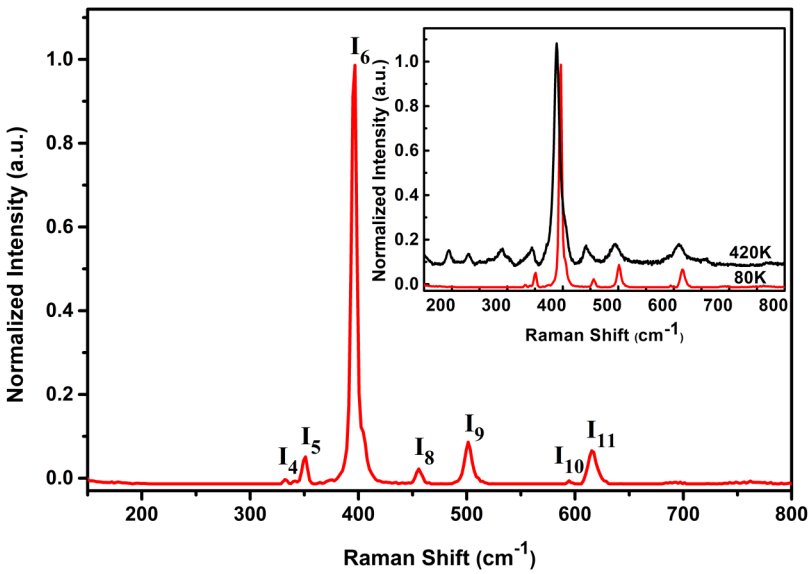

FIG. 7. Raman spectrum of Lu_2O_3 at 80 K.

Nd_2O_3[35] wherein the Raman spectra and the x-ray data displayed an anomalous shift in the diffraction peaks and attributed it to changes in the Nd–O bond length. The analogy in case of Lu_2O_3 may possibly be discussed in view of our previous report on the correlation of the behavior of the rare earth sesquioxides under pressure with the f electron number wherein it was deduced that the investigated rare earth oxides showed similar trends in structural transitions under pressure.[36] Since no other reports are available for the temperature-dependent variation in phonon modes, and considering the systematic increase in the intensity of the new modes mentioned above, it can be inferred conclusively that the cubic phase of Lu_2O_3 undergoes either an isostructural transition or a structural reorientation. However, no complete structural phase transition, wherein the crystalline structure changes, is observed up to the highest studied temperature of 420 K, and the cubic phase peaks are still existent.

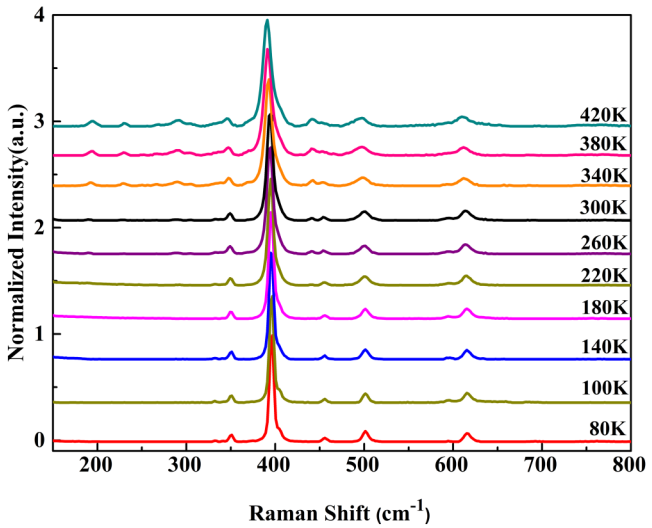

FIG. 8. Raman spectra of Lu_2O_3 for a temperature range from 80 K to 420 K.

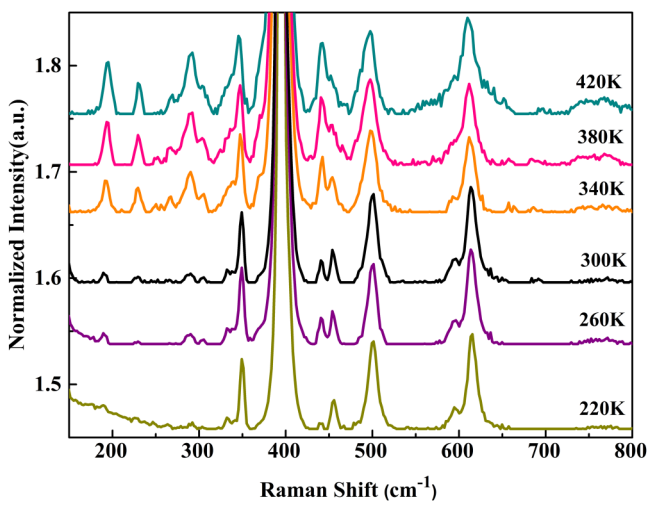

FIG. 9. Magnified view of the new phonon modes observed above 220 K.

TABLE III. Comparison of the peak position for various peaks at 80 K and 420 K.

Peak identification	Raman peak position at 80 K (cm^{-1})	Raman peak position at 420 K (cm^{-1})	Total shift (cm^{-1})
I_5	350.4	346.4	4.0
I_6	395.9	390.5	5.5
I_8	455.8	452.1	3.7
I_9	501.5	495.6	6.0
I_{11}	616.1	611.3	4.8

For these cubic phase peaks, the shifts observed from the starting temperature of 80 K to the maximum studied temperature of 420 K are shown in Table III. A maximum shift of 6.0 cm^{-1} is observed in the $F_g + A_g$ mode, designated as I_9, centered at 501.5 cm^{-1}. It may be pertinent to mention here that this mode also demonstrated the highest response to the application of pressure with the highest $d\omega/dp$ value, as shown in Table II.

It is well known that the shift in the phonon modes is dependent on the temperature and anharmonic contribution in the Hamiltonian.[37] Temperature-dependent phonon mode studies are used for quantization of anharmonicity. The shift in the frequency with the temperature is investigated in detail for the dominant peaks, i.e., for I_5, I_6, I_8, I_9, and I_{11}. The shifts occur due to the variation in the temperature, which leads to the lattice expansion or compression, depending upon the sample under investigation. Lattice expansion or compression is denoted by the positive or negative value of the thermal expansion coefficient, i.e., α of any material. The variation in the temperature also affects the frequency of the phonon due to anharmonic effects, which also contribute to the shift in the frequency of the phonon. Hence, phonon frequency[35] at any temperature is the sum of harmonic frequency, contribution in the frequency due to thermal volume expansion, and anharmonic contributions,

$$\omega(T) = \omega_0 + (\Delta\omega)_{latt} + (\Delta\omega)_{anh}, \tag{2}$$

where ω_0 is the harmonic frequency at 0K, $(\Delta\omega)_{latt}$ comes into play due to the lattice expansion, and $(\Delta\omega)_{anh}$ takes into account the cubic and quadric anharmonicity. ω_0 is calculated by extrapolation of the graph between the temperature and frequency of specific Raman modes to 0 K. $(\Delta\omega)_{latt}$ is given by

$$(\Delta\omega)_{latt} = \omega_0\left\{\exp\left[-\gamma_i\int_0^T 3\alpha(T)dT\right] - 1\right\}, \tag{3}$$

where γ_i represents the mode Grüneisen parameter, which shows the effect of varying temperature on the dynamics and size of the lattice. The value of α was taken from the literature[38] as 7.7×10^{-6}/K, while the value of γ_i has been calculated from our experiment, as explained above and also taken from available literature for comparison purposes.[23]

Furthermore, $(\Delta\omega)_{anh}$ is given by[37]

$$(\Delta\omega)_{anh} = A\left[1 + \frac{2}{\exp(\hbar\omega_0/2kT) - 1}\right] + B\left[1 + \frac{3}{\exp(\hbar\omega_0/3kT) - 1} + \frac{3}{(\exp(\hbar\omega_0/3kT) - 1)^2}\right]. \tag{4}$$

In the expression of $(\Delta\omega)_{anh}$, the first term represents the contribution due to the cubic term in the Hamiltonian or a three phonon process and the second term represents the contribution due to the quartic term in the Hamiltonian interaction of one phonon with three phonons, i.e., the four phonon process. The anharmonic constants, i.e., A and B, are found by fitting the graph between temperature and frequency using Eq. (2). The fitting was carried out for all the 5 peaks mentioned above. However, the fitting graph is shown here for the two most dominating peaks. It may be mentioned here that the three phonon process always results in the decrease in the phonon frequency, which results in the negative value of coefficient A. On the other hand, four phonon processes can increase as well as decrease the frequency of the phonon, i.e., coefficient B can be either positive or negative. In the present case, all the observable peaks show a similar trend of Raman shift vs temperature.

Figures 10 and 11 depict the variation in the phonon frequencies for the two representative modes. In the graphs, the squares represent the experimental data and the solid line represents the values obtained by the fitting equation. As expected, using the fitting equation, i.e., Eq. (2), the value of A comes out to be negative for all studied peaks while the value of B also comes out to be negative for all the studied peaks except for the mode I_{11}, which implies that in our case the four phonon process also results in the

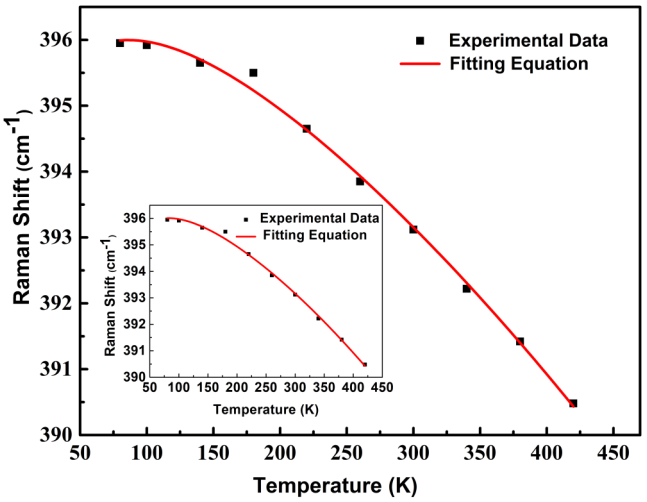

FIG. 10. Temperature dependence of the Raman shift, fitted using the calculated value of mode Grüneisen parameter for the phonon mode I_6. The inset shows the fitting using the value of γ_i from Ref. 23.

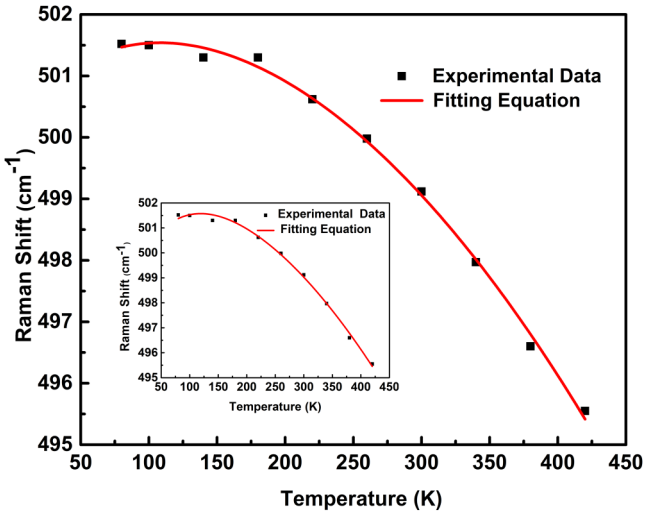

FIG. 11. Temperature dependence of the Raman shift, fitted using the calculated value of mode Grüneisen parameter for the phonon mode I_9. The inset shows the fitting using the value of γ_i from Ref. 23.

decrease in frequency except for mode I_{11}, for which it results in the positive contribution. In all the observed peaks, the anharmonic constant A has significantly higher values as compared to constant B, which implies that the three phonon processes are dominating for the temperature-driven response in most of the phonon modes. The values of anharmonic constants obtained are shown in Table IV. From Table IV and Figs. 10 and 11, it is also evident that for the calculations done using the value of γ_i from Ref. 23, the magnitudes of the constants A and B are impacted; however, the negative and positive components do not change sign.

Also, using the observed variations of the frequency with the temperature, the values of total anharmonicity and true anharmonic terms are also calculated. The value of total anharmonicity is given by[39]

$$\left(\frac{1}{\omega_i}\frac{d\omega_i}{dT}\right)_P = \left(\frac{1}{\omega_i}\frac{d\omega_i}{dT}\right)_V - \gamma_i \alpha. \tag{5}$$

The 1st term on the right hand side represents the true anharmonic term, and 2nd term represents the quasiharmonic term. The values obtained from the above equation are also shown in Table IV, i.e., the true anharmonic term, the quasianharmonic term, and the total anharmonicity for various Raman modes. From the table, it is apparent that owing to the lower value of the γ_i obtained from present studies, the quasiharmonic term has a lower value and, consequently, the true anharmonic term has a marginally higher magnitude.

The anharmonic effect also leads to the change in the bandwidth of the various Raman bands. The anharmonic effects result in either the decrease or increase of the FWHM. The effect of the anharmonic contribution on the FWHM is given by[37]

$$= \Gamma_o + C\left[1 + \frac{2}{\exp(\hbar\omega_0/2kT) - 1}\right] + D\left[1 + \frac{3}{\exp(\hbar\omega_0/3kT) - 1} + \frac{3}{(\exp(\hbar\omega_0/3kT) - 1)^2}\right], \tag{6}$$

where Γ_o represents the harmonic linewidth and the 2nd term represents the contribution due to the three phonon process; the 3rd part is due to the four phonon process. C and D represent the anharmonic constants.

The Raman modes obtained at each temperature were deconvoluted using the Voigt area fit in the Peak fit software for the temperature range of 80 K–420 K, and values of the FWHM were calculated for the various Raman modes. The variation of FWHM with temperature for the I_6 mode is plotted in Fig. 12. From this figure, it is clear that FWHM increases almost monotonically with an increase in the temperature. The solid line depicts the fitted curve using Eq. (6). From this fitting, the anharmonic constants C and D were found to have values of 2.6830 and −0.0290, respectively. It is clear that the 1st term of Eq. (4) dominates and is positive, which again implies that the three phonon term leads to broadening, while the negative value of the constant D suggests that the four phonon term has an opposite effect, albeit not significant.

Since phonons are quanta of lattice vibrations and the Raman modes correspond to the vibrations of the materials, hence, the lifetime of the phonon for various modes can be estimated using the

TABLE IV. Various parameters obtained using the fitting of temperature vs Raman shift data. The γ_i values taken from Ref. 23 are marked with an asterisk.

Peak identification	ω_0 (cm^{-1})	γ_i	A (cm^{-1})	B (cm^{-1})	$((1/\omega)^*d\omega/dT)_P$ (K^{-1})	$((1/\omega)^*d\omega/dT)_V$ (K^{-1})	$\Upsilon\alpha$ (K^{-1})
I_5	351.9	1.60*	−2.18	−0.17	-3.41×10^{-5}	-2.18×10^{-5}	1.23×10^{-5}
		1.30	−1.72	−0.18		-2.42×10^{-5}	0.99×10^{-5}
I_6	397.9	1.63*	−3.94	−0.17	-4.21×10^{-5}	-2.96×10^{-5}	1.26×10^{-5}
		1.35	−3.33	−0.19		-3.17×10^{-5}	1.04×10^{-5}
I_8	457.1	1.64*	−2.22	−0.51	-2.40×10^{-5}	-1.14×10^{-5}	1.26×10^{-5}
I_9	503.8	1.90*	−4.75	−0.68	-3.52×10^{-5}	-2.06×10^{-5}	1.46×10^{-5}
		1.22	−1.60	−0.92		-2.59×10^{-5}	0.93×10^{-5}
I_{11}	618.0	1.46*	−16.26	1.00	-2.47×10^{-5}	-1.35×10^{-5}	1.12×10^{-5}
		0.81	−9.70	0.30		-1.85×10^{-5}	0.62×10^{-5}

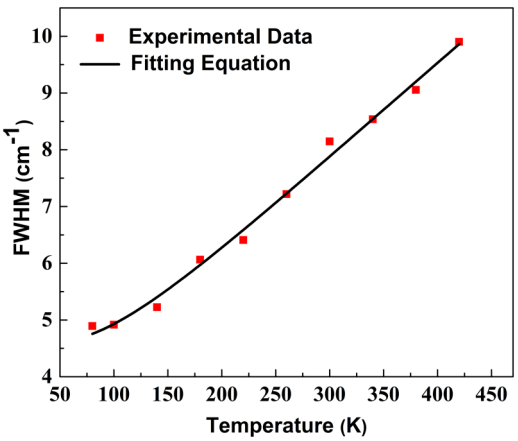

FIG. 12. Variation of the FWHM with increasing sample temperature.

Raman spectra. Raman spectroscopy is an indirect technique to calculate the phonon lifetime. The phonon lifetime is related to the FWHM by[40]

$$\tau = \frac{1}{\pi c \Gamma}, \tag{7}$$

where c is the velocity of light and Γ is the FWHM. The values obtained for phonon lifetimes for the most dominant Raman mode I_6 are calculated and plotted with the temperature in Fig. 13. As expected, the phonon lifetime decreases with an increase in temperature. The maximum lifetime of the phonon is 2.17 ps at 80 K and subsequently decreases with an increase in the temperature, which is evident due to the reason that FWHM increases with the temperature.

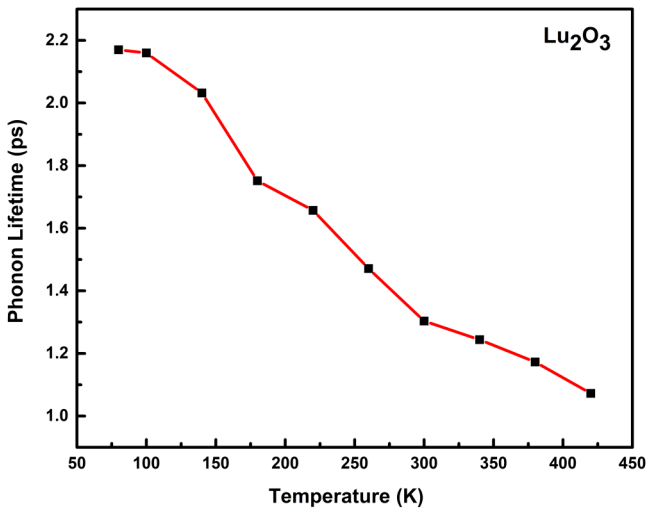

FIG. 13. Phonon lifetime for the F_g Raman mode.

CONCLUSIONS

The pressure and temperature-dependent Raman investigations on nanocrystalline Lu_2O_3 reveal that under the application of pressure, the cubic phase of the material is seen to be existent up to the highest studied pressure of about 15.6 GPa at a constant temperature and also up to a temperature of 420 K at a constant pressure. However, the cubic phase destabilized with an increase in pressure, and broad bands were seen to be developing beyond a pressure of about 7.0 GPa. These broad bands indicate the development of a disordered phase at the expense of the cubic phase. The mode Grüneisen parameter was calculated from the pressure data and, for our nanocrystalline sample, demonstrated a lower value as compared to the reported values for the bulk. Temperature-dependent Raman spectra at a constant pressure showed a softening of the phonon modes with an increase in the temperature. However, for temperatures above about 220 K, new cubic phase peaks were seen to develop that were not present at lower temperatures, which is an anomalous observation. The estimated anharmonic parameters reveal that the three phonon decay process dominates for most observed modes. The phonon lifetimes decreased with an increase in temperature.

ACKNOWLEDGMENTS

The authors are grateful to the Director, CSIR-NPL, for constant encouragement and to the Council of Scientific and Industrial Research (CSIR) as well as the University Grants Commission (UGC) for providing research fellowships under Grant Nos. 19/06/2016(i)EU-V and 1448|(CSIR- UGC NET DEC. 2017), respectively.

REFERENCES

[1]A. Sawada, T. Terai, A. Suzuki, and M. Yamawaki, "Fabrication of insulator coatings for fusion reactor liquid lithium blankets," J. Phys. Chem. Solids **66**(2–4), 681–683 (2005).
[2]B. Aktas, S. Tekeli, and M. Kucuktuvek, "Grain growth and sinterability in Er_2O_3-doped cubic zirconia (c-ZrO_2)," Int. J. Mater. Res. **105**, 208 (2014).
[3]Y. Wang, G. Zhu, S. Xin, Q. Wang, Y. Li, W. Quansheng, C. Wang, X. Wang, X. Ding, and W. Geng, "Recent development in rare-earth-doped phosphors for white light-emitting diodes," J. Rare Earths **33**, 1–12 (2015).
[4]L. Fornasiero, E. Mix, V. Peters, K. Petermann, and G. Huber, "New oxide crystals for solid state lasers," Cryst. Res. Technol. **34**, 255–260 (1999).
[5]K. Eguchi, "Ceramic materials containing rare earth oxides for solid oxide fuel cell," J. Alloys Compd. **250**, 486–491 (1997).
[6]G. Hass, J. B. Ramsey, and R. Thun, "Optical properties of various evaporated rare earth oxides and fluorides," J. Opt. Soc. Am. **49**, 116–120 (1959).
[7]H. R. Hoekstra, "Phase relationships in the rare earth sesquioxides at high pressure," Inorg. Chem. **5**, 754 (1966).
[8]L. A. Tucker, F. J. Carney, Jr., P. McMillan, S. H. Lin, and L. Eyring, "Raman and resonance Raman spectroscopy of selected rare-earth sesquioxides," Appl. Spectrosc. **38**(6), 857–860 (1984).
[9]A. G. Dedov, A. S. Loktev, I. I. Moiseev, A. Aboukais, J.-F. Lamonier, and I. N. Filimonov, "Oxidative coupling of methane catalyzed by rare earth oxides: Unexpected synerigistic effect of the oxide mixtures," Appl. Catal. A **245**, 209 (2003).
[10]A. Garcia-Murillo, C. LeLuyer-Urlacher, C. Dujardin, C. Pédrini, and J. Mugnier, "Rare-earth actived sol-gel films for scintillator applications," J. Sol Gel Sci. Technol. **26**, 957–960 (2003).

[11]J. Yang, C. Zhang, C. Peng, C. Li, L. Wang, R. Chai, and L. Jun, "Controllable red, green, blue (RGB) and bright white upconversion luminescence of Lu_2O_3: $Yb^{3+}/Er^{3+}/Tm^{3+}$ nanocrystals through single laser excitation at 980 nm," Chem. Eur. J. **15**, 4649–4655 (2009).
[12]I. J. Graumann, A. Diebold, C. G. E. Alfieri, F. Emaury, B. Deppe, M. Golling, D. Bauer, D. Sutter, C. Kränkel, C. J. Saraceno, C. R. Phillips, and U. Keller, "Peak-power scaling of femtosecond Yb:Lu_2O_3 thin-disk lasers," Opt. Express **25**, 22519 (2017).
[13]W. Barrera, C. Cascales, M. Cinta Pujol, K. H. Park, S. B. Choi, F. Rotermund, J. J. Carvajal, X. Mateos, M. Aguiló, and F. Díaz, "Synthesis of Tm:Lu_2O_3 nanocrystals for phosphor blue applications," Phys. Procedia **8**, 142–150 (2010).
[14]A. M. Heuer, P. Von Brunn, G. Huber, and C. Kränkel, "Dy^{3+}:Lu_2O_3 as a novel crystalline oxide for mid-infrared laser applications," Opt. Mater. Express **8**, 3447 (2018).
[15]A. García-Murillo, C. Le Luyer, C. Dujardin, T. Martin, C. Garapon, C. Pédrini, and J. Mugnier, "Elaboration and scintillation properties of Eu^{3+}-doped Gd_2O_3 and Lu_2O_3 sol-gel films," Nucl. Instrum. Methods Phys. Res. Sect. A **486**, 181–185 (2002).
[16]S. Ohmi, M. Takeda, H. Ishiwara, and H. Iwai, "Electrical characteristics for Lu_2O_3 thin films fabricated by E-beam deposition method," J. Electrochem. Soc. **151**, G279 (2004).
[17]A. F. Goncharov, "Raman spectroscopy at high pressures," Int. J. Spectrosc. **2012**, 617528.
[18]M. Guzik, J. Pejchal, A. Yoshikawa, A. Ito, T. Goto, M. Siczek, T. Lis, and G. Boulon, "Structural investigations of Lu_2O_3 as single crystal and polycrystalline transparent ceramic," Cryst. Growth Des. **14**, 3327–3334 (2014).
[19]L. Marsella and V. Fiorentini, "Structure and stability of rare-earth and transition metal oxides," Phys. Rev. B **69**, 172103 (2014).
[20]L. An, A. Ito, and T. Goto, "Fabrication of transparent lutetium oxide by spark plasma sintering," J. Am. Ceram. Soc. **94**(3), 695–698 (2011).
[21]P. Delugas and V. Fiorentini, "Dielectric properties of two phases of crystalline lutetium oxide," Microelectron. Reliab. **45**, 831–833 (2005).
[22]Y. Zhang, "Thermodynamic properties of rare earth sesquioxides," Ph.D. thesis, McGill University, Montreal, QC, Canada, 2016.
[23]S. Jiang, J. Liu, C. Lin, L. Bai, W. Xiao, Y. Zhang, D. Zhang, X. Li, Y. Li, and L. Tang, "Pressure induced phase transition in cubic Lu_2O_3," J. Appl. Phys. **108**, 083541 (2010).
[24]C.-M. Lin, K.-T. Wu, T.-L. Hung, H.-S. Sheu, M.-H. Tsai, J.-F. Lee, and J.-J. Lee, "Phase transitions in Lu_2O_3 under high pressure," Solid State Commun. **150**, 1564–1569 (2010).
[25]W. B. White and V. G. Keramidas, "Vibrational spectra of oxides with the c-type rare earth oxides structure," Spectrochim. Acta **28**, 501–509 (1972).
[26]A. A. Kaminskii, S. N. Bagaev, H. J. Eichler, K. Ueda, K. Takaichi, A. Shirakawa, H. Yagi, T. Yanagitani, and H. Rhee, "Observation of high-order Stokes and anti-Stokes $\chi^{(3)}$-generation in highly transparent laser-host Lu_2O_3 ceramics," Laser Phys. Lett. **3**, 310 (2006).
[27]M. V. Abrashev, N. D. Todorov, and J. Geshev, "Raman spectra of R_2O_3 (R-rare earth) sesquioxides with C-type bixbyite crystal structure: A comparative study," J. Appl. Phys. **116**, 103508 (2014).
[28]Y. Jinqiu, C. Lei, H. Huaqiang, Y. Shihong, H. Yunsheng, and Wu-Hao, "Raman spectra of RE_2O_3 (RE = Eu, Gd, Dy, Ho, Er, Tm, Yb, Lu, Sc and Y): Laser-excited luminescence and trace impurity analysis," J. Rare Earths **32**(1), 1 (2014).
[29]L. Laversenne, Y. Guyot, C. Goutaudier, M. T. Cohen-Adad, and G. Boulon, "Optimization of spectroscopic properties of Yb^{3+}-doped refractory sesquioxides: Cubic Y_2O_3, Lu_2O_3 and monoclinic Gd_2O_3," Opt. Mater. **16**, 475–483 (2001).
[30]S. Klotz, J.-C. Chervin, P. Munsch, and G. Le Marchand, "Hydrostatic limits of 11 pressure transmitting media," J. Phys. D Appl. Phys. **42**, 075413 (2009).
[31]N. Dilawar, D. Varandani, S. Mehrotra, H. K. Poswal, S. Sharma, and A. K. Bandyopadhyay, "Anomalous high pressure behaviour in nanosized rare earth sesquioxides," Nanotechnology **19**, 115703 (2008).
[32]B. Liu, B. Liu, Q. Li, Z. Li, M. Yao, R. Liu, X. Zou, H. Lv, W. Wu, W. Cui, Z. Liu, D. Li, B. Zou, T. Cui, and G. Zou, "High-pressure Raman study on CeO_2 nanospheres self-assembled by 5 nm CeO_2 nanoparticles," Phys. Status Solidi B **248**(5), 1154–1157 (2011).
[33]G. Lucazeau, "Effect of pressure and temperature on Raman spectra of solids: Anharmonicity," J. Raman Spectrosc. **34**, 478–496 (2003).
[34]R. N. Compton and N. I. Hammer, "Raman under liquid nitrogen (RUN)," J. Phys. Conf. Ser. **548**, 012017 (2014).
[35]S. Jiang, J. Liu, L. Bai, X. Li, Y. Li, S. He, S. Yan, and D. Liang, "Anomalous compression behavior in Nd_2O_3 studied by x-ray diffraction and Raman spectroscopy," AIP Adv. **8**, 025019 (2018).
[36]N. D. Sharma, J. Singh, A. Vijay, K. Samanta, S. Dogra, and A. K. Bandyopadhyay, "Pressure-induced structural transition trends in nanocrystalline, rare-earth sesquioxides: A Raman investigation," J. Phys. Chem. C **120**(21), 11679–11689 (2016).
[37]M. Balkanski, R. F. Wallis, and E. Haro, "Anharmonic effects in light scattering due to optical phonons in silicon," Phys. Rev. B **28**(4), 1928 (1983).
[38]A. Pavlik III, S. V. Ushakov, A. Navrotsky, C. J. Benmore, and R. J. K. Weber, "Structure and thermal expansion of Lu_2O_3 and Yb_2O_3 up to the melting points," J. Nucl. Mater. **495**, 385–391 (2017).
[39]B. A. Weinstein and R. Zallen, in *Light Scattering in Solids IV*, edited by M. Cardona and G. Guntherodt (Springer-Verlag, Berlin, 1984), p. 463.
[40]K. Samanta, P. Bhattacharya, and R. S. Katiyar, "Temperature dependent E_2 Raman modes in the ZnCoO ternary alloy," Phys. Rev. B **75**, 035208 (2007).